5-22-2012

Cumulative Lesioning of Respiratory Interneurons Disrupts and Precludes Motor Rhythms in Vitro

Xueying Wang
College of William and Mary

John A. Hayes
College of William and Mary, jahaye@wm.edu

Christopher A. Del Negro
College of William and Mary, cadeln@wm.edu

Recommended Citation

Wang, Xueying; Hayes, John A.; and Del Negro, Christopher A., Cumulative Lesioning of Respiratory Interneurons Disrupts and Precludes Motor Rhythms in Vitro (2012). *PNAS*, 109(21). https://doi.org/10.1073/pnas.1200912109

Cumulative lesioning of respiratory interneurons disrupts and precludes motor rhythms in vitro

John A. Hayes[a,b,1,2], Xueying Wang[a,2], and Christopher A. Del Negro[a,3]

Departments of [a]Applied Science and [b]Biology, College of William and Mary, Williamsburg, VA 23187-8795

Edited by Eve Marder, Brandeis University, Waltham, MA, and approved April 10, 2012 (received for review January 19, 2012)

How brain functions degenerate in the face of progressive cell loss is an important issue that pertains to neurodegenerative diseases and basic properties of neural networks. We developed an automated system that uses two-photon microscopy to detect rhythmic neurons from calcium activity, and then individually laser ablates the targets while monitoring network function in real time. We applied this system to the mammalian respiratory oscillator located in the pre-Bötzinger Complex (preBötC) of the ventral medulla, which spontaneously generates breathing-related motor activity in vitro. Here, we show that cumulatively deleting preBötC neurons progressively decreases respiratory frequency and the amplitude of motor output. On average, the deletion of 120 ± 45 neurons stopped spontaneous respiratory rhythm, and our data suggest ≈82% of the rhythm-generating neurons remain unlesioned. Cumulative ablations in other medullary respiratory regions did not affect frequency but diminished the amplitude of motor output to a lesser degree. These results suggest that the preBötC can sustain insults that destroy no more than ≈18% of its constituent interneurons, which may have implications for the onset of respiratory pathologies in disease states.

central pattern generator | calcium imaging | brainstem

Central pattern generator (CPG) networks produce coordinated motor patterns that underlie behaviors such as breathing, locomotion, and chewing (1, 2). A key issue is not just which cell types generate these patterns of activity, but how many? This question pertains to whether and how cumulative cell loss will impair and, possibly preclude, network function.

Breathing consists of inspiratory and expiratory phases. The pre-Bötzinger Complex (preBötC) of the medulla putatively contains the inspiratory CPG (3, 4). Over several days in vivo, saporin-mediated destruction of preBötC neurons that express neurokinin-1 receptors (NK1Rs) causes sleep-disordered breathing and fatal respiratory pathology (5, 6). Similarly, acute cell-silencing of a subset of the same NK1R-expressing population of preBötC neurons stops spontaneous breathing in awake adult rats (7). These studies helped to determine the cellular composition of the preBötC and confirmed that it was essential for breathing in an otherwise intact animal, but could not measure the resiliency of the preBötC when faced with silencing or deleting its core piecewise.

We examined this issue by using slice preparations that capture the preBötC and spontaneously generate fictive breathing-related activity in vitro. We developed a computer-automated system that detects rhythmically active interneurons via two-photon calcium imaging, stores their physical locations in memory, and then laser ablates the targets sequentially, while electrophysiologically monitoring the motor output of the circuit. We applied this system to the preBötC to test the hypothesis that piecewise destruction of the CPG core would cause graded loss of motor activity up to rhythm cessation. We surmised that this effect would occur principally via changes in cycle period. However, we observed two main effects. The cumulative deletion of preBötC interneurons diminished the amplitude of respiratory motor output and caused an increase in the cycle period that led inexorably to rhythm cessation. These data suggest that preBötC neurons coordinate both periodicity and premotor drive. Our measurements provide an upper limit for tolerance to cell destruction in a mammalian CPG.

Results

Breathing-related neurons form a ventral respiratory column (VRC) that begins caudal to the facial nucleus (VII) and extends to the cervical spinal cord. Contiguous respiratory nuclei serve different functions. The inspiratory phase of breathing is generated by interneurons within the bilaterally distributed preBötC (3–5, 7, 8). Slice preparations that capture the preBötC generate inspiratory-related rhythms in vitro that are measurable as motor output from the hypoglossal (XII) nerve rootlets (Fig. 1*A*).

We examined network properties in the preBötC by deleting its constituent interneurons, one cell at a time, while monitoring function via the XII nerve. In our setup, one master computer controls a Ti:sapphire long-wavelength laser, a laser-scanning microscope, and a robotic X-Y stage control system, while another time-synced workstation continuously monitors XII output. The experiments consist of a detection phase that maps populations of respiratory neurons in the bilateral volumes of the slice, followed by an ablation phase wherein target neurons are sequentially laser ablated.

Detecting Inspiratory Neurons in the preBötC and Ventral Respiratory Column. We implemented two cutting strategies to prepare transverse slices that both retain the preBötC and expose inspiratory-modulated neurons at the slice surface. The geometry of the first slice type exposed the VRC at least 100 μm rostral to the preBötC (i.e., a VRC-surface slice), whereas the second type exposed the preBötC at its rostral face (i.e., a preBötC-surface slice; Fig. 2). Slices were calibrated online according to an atlas (9). After cutting, slices were incubated with the calcium-sensitive indicator Fluo-8 AM to detect rhythmic inspiratory activity (Figs. 1*B* and 3 and Figs. S1 and S2). We were able to image to a depth of 80 μm by using Ti:sapphire laser pulses in both slice types. Synaptic inhibition is not essential for rhythmogenesis in vitro, but it influences the amplitude of XII output (10, 11). Therefore, we added 5 μM strychnine and picrotoxin to the artificial cerebrospinal fluid (ACSF) before the detection phase so that XII output would be insensitive to the effects of laser-ablating inhibitory neurons (12, 13) during the ablation phase.

Inspiratory neurons could be identified bilaterally by an automated routine that acquires 1 min of calcium imaging data from

Author contributions: J.A.H. and C.A.D.N. designed research; J.A.H. and X.W. performed research; J.A.H. and X.W. contributed new reagents/analytic tools; J.A.H., X.W., and C.A.D.N. analyzed data; and J.A.H. and C.A.D.N. wrote the paper.

The authors declare no conflict of interest.

This article is a PNAS Direct Submission.

Freely available online through the PNAS open access option.

[1]Present address: Neurobiologie et Développement, Institut de Neurobiologie Alfred Fessard, Centre National de la Recherche Scientifique, 91198 Gif-sur-Yvette, France.

[2]J.A.H. and X.W. contributed equally to this work.

[3]To whom correspondence should be addressed. E-mail: cadeln@wm.edu.

This article contains supporting information online at www.pnas.org/lookup/suppl/doi:10.1073/pnas.1200912109/-/DCSupplemental.

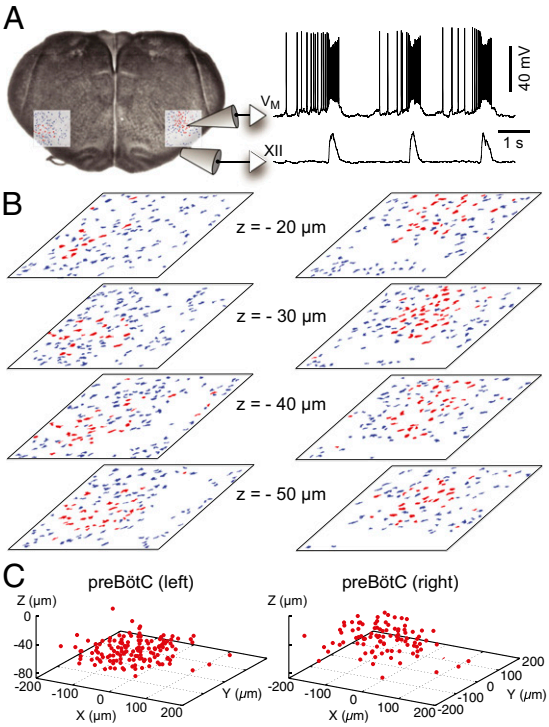

Fig. 1. Inspiratory neurons in the preBötC. (*A*) Rhythmically active neurons identified bilaterally by imaging. Whole-cell recording (upper trace) with XII motor output (lower trace). (*B*) Mask of targets showing inspiratory (red) and noninspiratory neurons (blue) for focal planes (20–50 μm shown here). (*C*) 3D reconstruction of detected targets for all focal planes 0–70 μm (also see Fig. S1), where each inspiratory neuron is represented by a single point at the soma.

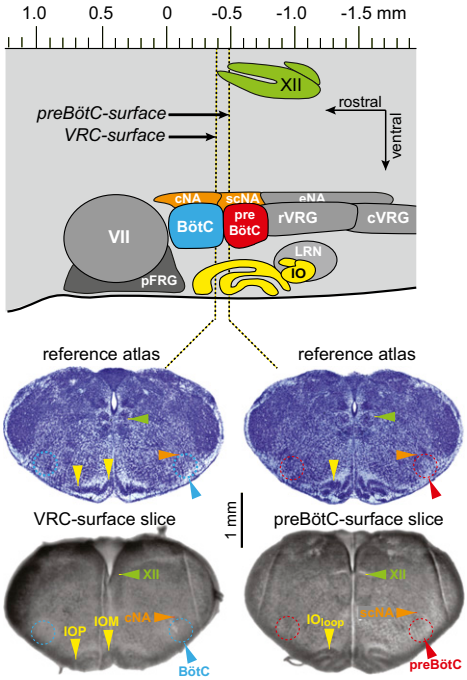

Fig. 2. Anatomy of slices that retain the preBötC. Parasagittal view (top) shows nuclei that comprise the ventral respiratory column (VRC): Bötzinger complex (BötC), preBötzinger complex (preBötC), rostral and caudal ventral respiratory group (rVRG and cVRG), facial nucleus (VII), and the parafacial respiratory group (pFRG). Also shown are the compact, semicompact, and external (loose) formations of the nucleus ambiguous (cNA, scNA, and eNA). The hypoglossal nucleus (XII) is shown dorsally. The principal and medial divisions of the inferior olive (IOP and IOM), and the visible loop (IO_{loop}), are located, with the lateral reticular nucleus (LRN), ventral to the VRC. The axis (*Top*) is reproduced from brainstem atlas for newborn mice; preBötC-surface (*Bottom Right*) and VRC-surface (*Bottom Left*) slices are shown with reference images (*Middle*) (9).

the preBötC at each 10-μm increment of depth and then computes the SD of fluorescence through the image stacks (Fig. 3 *A* and *B*). Because regions of interest (ROIs) with high SD may represent oscillatory neurons, each one was added to a mask of potential targets and assigned a unique index (Fig. 3 *C* and *D*). Fluorescence changes (ΔF), or fluorescence changes with respect to baseline ($\Delta F/F_0$), were computed as a time series for each ROI, and a relative power spectrum density graph was plotted by using Fourier analysis. If a time series showed significant power in the frequency range associated with respiratory rhythm in vitro, 0.15–0.5 Hz (Fig. 3 *E* and *F*), then it was accepted as a bona fide inspiratory neuron. If peak power fell outside the range 0.15–0.5 Hz, then the cell was rejected (Fig. 3*G*). Rhythmic calcium transients reliably identify inspiratory neurons (14). Nevertheless, we performed whole-cell recordings from neurons identified by the routine above, which all showed inspiratory activity ($n = 3$) (Fig. 3 *H–L*).

The system evaluates each ROI to arrive at a final mask of inspiratory cell targets. Inspiratory neurons occupied a circular region 150–200 μm in diameter in the ventrolateral margins of the slice, which is characteristic of nuclei throughout the VRC, including—but not limited to—the preBötC (Figs. S1 and S2). Detection was repeated bilaterally at all resolvable depths (Fig. S3). PreBötC-surface slices showed 9 ± 5 (mean ± SD) rhythmic neurons per 10-μm plane per side ($n = 5$ slices; Table S1), whereas VRC-surface slices showed 12 ± 9 inspiratory neurons per plane per side ($n = 8$ slices; Table S2) ($P = 0.2$, Mann–Whitney u test).

Single-Cell Laser Ablation and Confirmation. Inspiratory neurons were randomly selected from the 3D collection of targets (Fig. 1*C*) and subjected to laser ablation, one cell at a time. The Ti:sapphire laser was focused on the target and then scanned over a 110-μm^2 subregion at the center of the ROI with 800-nm pulses at full intensity, while acquiring an image in the band 560–615 nm. The lesion was confirmed by analyzing the image: A threshold-crossing algorithm can detect presumed water vapor in the cell cavity while excluding green dye emissions and infrared reflections from the laser. Additionally, ablated targets vanished from the calcium fluorescence images (Fig. 3*M*). Infrared-enhanced differential interference contrast (IR-DIC) imaging showed that in successful lesions, a pockmark replaced the original cell image (Fig. 3*N*). Lesion confirmation was obtained $91 \pm 1\%$ of the time ($n = 2{,}331$ attempts in $n = 13$ slices). Only confirmed lesions were added to the tally. After each ablation, the system randomly selected another target and attempted another lesion. The stage was left-right alternated after every 50th lesion. The system looped between target selection and laser ablation until the whole 3D set of targets was exhausted bilaterally.

Ablation of Inspiratory Neurons from the Ventral Respiratory Column. VRC-surface slices and preBötC-surface slices function indistinguishably from the standpoint of XII motor output because both slices retain the necessary and sufficient medullary circuits to generate spontaneous respiratory rhythms in vitro (9, 15). However, these two cutting strategies expose different respiratory circuits at the rostral face of the slice. VRC-surface slices expose respiratory neurons rostral to the preBötC, in a region that includes the Bötzinger complex (BötC) (16, 17), which is not associated with inspiratory rhythmogenesis. We hypothesized that cumulative ablation of VRC inspiratory neurons would not affect cycle period or stop rhythmogenesis.

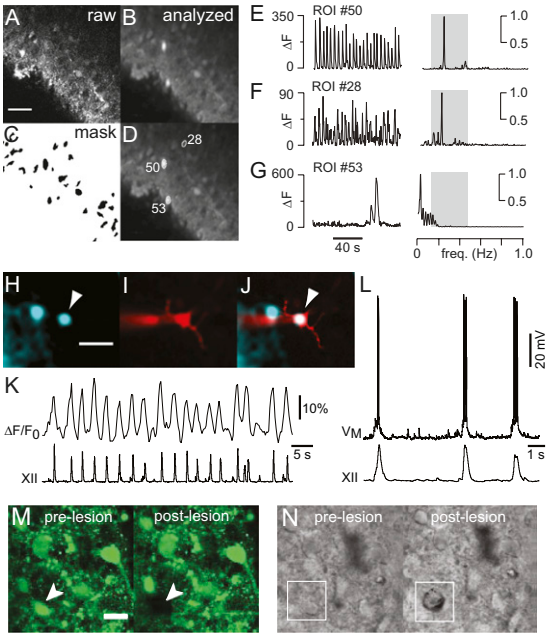

Fig. 3. Neuron detection and ablation. (*A*) One frame of raw fluorescence. (*B*) SD of fluorescence through 2-min stack. (*C*) Mask of putative target cells. (*D*) Detected cells displayed with ROIs and numeric indices. (*E*–*G*) Time- and frequency-domain analyses. ΔF was plotted to emphasize differences in the amplitude of the fluorescence signals. (*E*) Inspiratory neuron (#50). (*F*) Inspiratory neuron (#28). (*G*) Nonrespiratory neuron (#53). (*H*) Inspiratory neuron (arrowhead) detected automatically by the software. Cyan-green pseudocolor shows SD of Fluo-8 AM activity. (*I*) Neuron in *H* filled with Alexa 568 from the patch pipette. (J) Merged image. (*K*) $\Delta F/F_0$ activity from the cell in *H*–*J* with XII output. (*L*) Whole-cell recording from the cell in *H*–*K* with XII output. (Scale bars: *A* and *H*: 40 μm.) (*M*) Pre- and postlesion images of Fluo-8 AM labeled neurons in the preBötC. Arrowhead shows the target cell. (*N*) Pre- and postlesion images in IR-DIC with the target cell outlined in white. (Scale bars: *M* and *N*, 20 μm.)

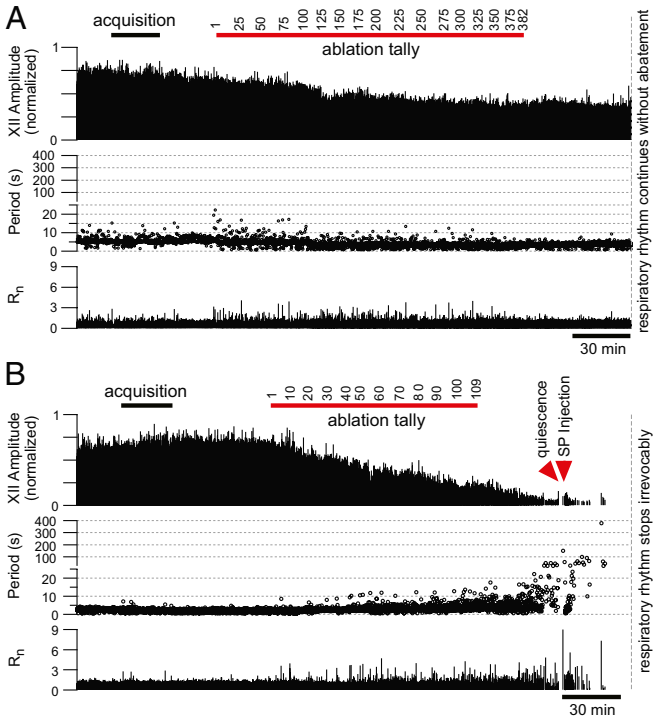

Fig. 4. Cumulative deletion of inspiratory neurons. (*A* and *B*) The *x* axis is a timeline. The *y* axis plots XII amplitude (normalized units; *Top*), respiratory period (*Middle*), and regularity score (R_n) (*Bottom*). The respiratory period axis is continuous (0–400 s) but plotted with two scales. Major ticks are separated by 5 s from 0 to 25 s and, thereafter, major ticks are plotted in 100-s divisions from 26 to 400 s. Period and regularity axes plot a data point for every instantaneous period measured. The recording in *B* stops after 10 min of XII quiescence. (*A*) Ablating inspiratory neurons in a VRC-surface slice preparation. (*B*) Ablating inspiratory neurons in a preBötC-surface slice preparation with SP injection (right red triangle).

We ablated 192 ± 80 inspiratory neurons in VRC-surface slices (n = 8; Fig. 4*A*). The magnitude of the XII output always measured ≥50% of its control during the ablation phase (Fig. 5*A*). On average, the XII output measured 76 ± 7% of control during the postlesion epoch (32 min of continuous recording after the final target ablation; Fig. 5*B*). Respiratory cycle period did not change significantly during the ablation phase or during the postlesion epoch (Fig. 5 *C* and *D*). Cycle period measured 5.2 ± 0.3 s during the prelesion epoch and 4.3 ± 0.3 s during the postlesion epoch (P = 0.07, paired Student's t test). Additionally, the coefficient of variation (CV) of prelesion periods (0.41 ± 0.04) was not significantly different from the postlesion CV (0.33 ± 0.04) (P = 0.13, paired Student's t test; Fig. 5*E*). The regularity score (R_n), which measures fluctuations in period, settled at ≈1 after the ablation phase, which implies nominally perfect regularity (Fig. 4*A*). These data show that cumulative ablation of inspiratory neurons outside of the preBötC does not perturb or stop respiratory rhythm, although the amplitude of XII motor output declines.

Ablation of Inspiratory Neurons in preBötC. The outcome was different in preBötC-surface slices (n = 5, Fig. 4*B*). Cumulative single-cell laser ablations decreased the amplitude of XII output and respiratory frequency (Fig. 5 *A*–*D*) and, ultimately, stopped the rhythm (Figs. 4*B* and 6*A*). During the ablation phase in preBötC-surface slices, the amplitude of XII motor output declined −0.6% per neuron deleted, whereas in VRC-surface slices, it declined −0.16% per neuron deleted (P = 0.001, Mann–Whitney u test; Fig. 5*A*). The amplitude of XII motor output of preBötC-surface slices declined to 37 ± 7% of control during the postlesion epoch, which was significantly greater than the XII decline measured similarly postlesion in VRC-surface slices (P = 0.002, unpaired Student's t test; Fig. 5*B*).

The cycle period increased during the course of lesioning (Fig. 5*C*) and continued to increase after lesion targets were exhausted (reaching 120–200 s, Figs. 4*B* and 6*A*). The mean period for the postlesion epoch was 25 ± 12 s, which compared with 3.4 ± 0.4 s before lesion, was statistically significant (P = 0.008, Mann–Whitney u test; Fig. 5*D*). Postlesion periods formed a unimodal long-tail distribution, which is inconsistent with quantal slowing (8). The CV for cycle period changed significantly from 0.5 ± 0.1 before lesion to 1.3 ± 0.3 during the postlesion epoch (P = 0.02, Mann–Whitney u test; Fig. 5*E*). Unlike VRC-surface slices that reestablished regularity after the ablation phase, preBötC-surface slices showed large cycle-to-cycle fluctuations in period that are reflected in R_n measurements in the range of 1–9 after the ablation phase (Fig. 4).

On average, the confirmed deletion of 120 ± 45 preBötC neurons (mean ± SD) resulted in rhythm cessation 32 ± 2 min (mean ± SEM) after the final cell ablation. We continued to monitor XII activity to confirm that rhythm never recovered spontaneously within a 2- to 3-h range (n = 5).

Transiently Rescuing Rhythmic, but Irregular, preBötC Activity. The data in Figs. 4 and 5 suggest that the cumulative deletion of inspiratory neurons in preBötC-surface slices had a profound effect on XII output and caused a catastrophic change in the CPG that degraded and destabilized its rhythmogenic capability.

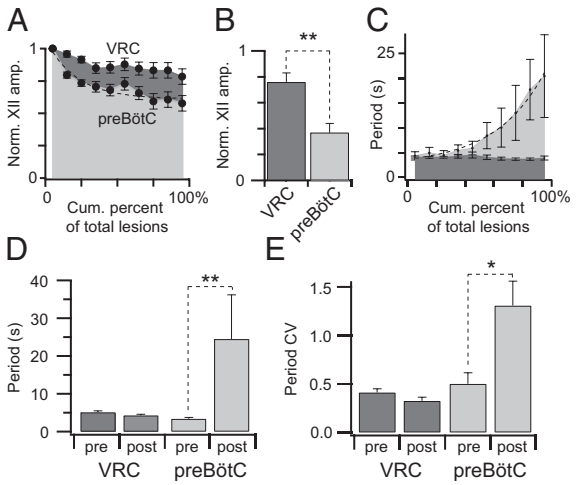

Fig. 5. Ablation effects on respiratory rhythm and XII amplitude. Measurements are displayed in light gray for preBötC-surface slices and dark gray for VRC-surface slices. (*A*) XII amplitude vs. cumulative percent of total lesions. (*B*) Postlesion changes in XII amplitude (**P = 0.001). (*C*) Cycle periods vs. cumulative percent of total lesions. A dashed exponential function is fit to the cycle period data for preBötC-surface slices. (*D*) Mean cycle period for pre- and postlesion epochs, (**P = 0.008). (*E*) Mean CV for pre- and postlesion epochs (*P = 0.02).

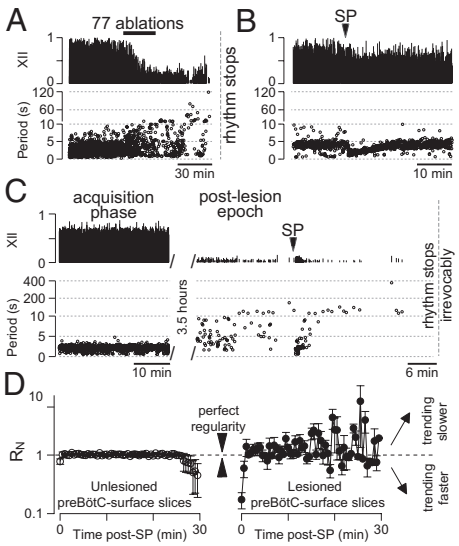

Fig. 6. SP injections in preBötC-surface slices. (*A*) Lesioned preBötC-surface slice without SP injection. (*B*) Unlesioned preBötC-surface slice injected with a bolus of SP. (*C*) Lesioned preBötC-surface slice shown in the acquisition phase (*Left*) and 3.5 h later during the postlesion epoch (*Right*). (*D*) R_n binned in 0.5-min increments for unlesioned preBötC-surface slices (*Left*; n = 4) and lesioned preBötC-surface slices (*Right*; n = 5) after SP injection at t = 0. Values approaching one are increasing in regularity whereas values greater than or less than unity are becoming more irregular.

However, another explanation could involve a loss of excitatory drive, wherein the ablation of rhythmic neurons that support CPG function via neuromodulation reduce preBötC excitability. Monoaminergic and peptidergic projections maintain excitability in the preBötC, and exogenous substance P (SP) stimulates the preBötC by acting on the core population of NK1R-expressing rhythmogenic interneurons (18). Monoaminergic and peptidergic neurons also receive feedback projections from the preBötC, which endows them with respiratory rhythmicity and makes them susceptible to loss of input due to the cumulative laser ablation protocol. To test the idea that lesions reduce excitability, we injected a bolus of SP into the preBötC after the respiratory cycle period exceeded 120 s, which we empirically determined was a reliable benchmark of a slice that, without SP injection, would cease rhythmic function within 5–10 min (Fig. 6*A*).

Slices bathed in 9 mM K^+ ACSF typically exhibit a cycle period of ≈5 s. In four unlesioned control slices, bolus injection of 1 mM SP transiently lowered the cycle period to 2.2 ± 0.2 s (mean ± SEM, computed for 25 cycles), which remained <5 s for 13 ± 1 min (Fig. 6*B*). In five lesioned slices, bolus SP injection revived activity transiently. The average cycle period was 1.8 ± 0.2 s (mean ± SEM, computed for 10 cycles), which remained <5 s for 5 ± 1 min (Fig. 6*C*). Judged by the duration that the cycle periods remained <5 s, the SP effect was significantly shorter in lesioned preBötC-surface slices (P = 0.002, unpaired Student's t test). Furthermore, lesioned slices did not continue rhythmic output indefinitely after the effects of the SP injection subsided, whereas unlesioned controls maintained rhythmicity for 4–6 h. More importantly, the SP-evoked rhythmic activity was irregular, whereas unlesioned controls maintained nearly perfect regularity scores after SP injection (Fig. 6*D*). These data suggest that NK1R-expressing preBötC neurons can generate irregular cycles after lesion if suitably modulated but cannot sustain regular rhythmogenesis.

Discussion

Here, we present an automated laser detection and ablation system that can destroy a well-defined cell class, while neighboring neurons, glia, and axons in passing are left unharmed. The preparation can be monitored in vitro throughout the process. We applied this system to elucidate network properties of the preBötC.

Advantages of Cell-Specific Laser Detection and Ablation. Laser ablation has been applied to study locomotor networks. In zebrafish cyan (488-nm) laser exposure for 10–12 min photoablated reticulospinal neurons by augmenting the toxicity of indicator dyes, revealing specific roles for Mauthner cells and their homologs in short-latency escape behaviors (19). UV lasers (≈400 nm) were used in *Caenorbabditis elegans* to investigate locomotion, chemotaxis, and mechanosensation (20). Cell killing required several minutes of laser exposure and often damaged surrounding tissues. In zebrafish and *C. elegans*, prior knowledge of cell locations was required to ablate the targets manually. The system we developed does not require a priori knowledge of target cell locations. The map of targets is generated online, and measurable cell function is the principal selection criterion. Laser ablation is fast; each lesion can be accomplished in 2–16 s. These features are important for applicability in mammalian networks where there may be hundreds of cell targets, and aside from general neuroanatomical guidelines, the specific map of targets is unknown beforehand.

Viral transfection can be used to silence neuron populations (21). Knockout mice also remove cell classes wholesale rather than piecewise. These techniques operate at the whole-population level and have proven helpful in answering questions regarding which cells generate a particular behavior. However, such techniques do not allow cellular-level quantitative analyses of lesion effects on behavior. Similarly, the toxin saporin causes graded cell destruction over several days, but it is impossible to keep a running tally of cell destruction in vivo while monitoring behavioral changes (5, 6). We developed the present system for slices that retain behaviorally relevant function and expose CPG interneurons. Single-cell ablations elicit real-time feedback to address the question: How many neurons contribute to sustaining network function?

Structure and Function of the preBötC. In both slice types, the amplitude of XII output decreased as a function of lesion tally. Nevertheless, the XII amplitude decreased more in preBötC-surface slices, which suggests that the preBötC has some premotor

function and does not perform a purely rhythmogenic clock-like function. This conclusion is consistent with whole-cell recordings demonstrating that excitatory drive from the preBötC is conserved in XII premotor circuits (15).

Respiratory period and CV increased in preBötC-surface slices as the lesion tally increased. Cycle period and CV did not show similar changes in VRC-surface slices. We conclude that respiratory period and its regularity are directly related to the number of rhythmogenic neurons in the preBötC. However, the cycle period continued to lengthen after the lesioning stopped, with rhythm cessation occurring after ≈30 min. What causes this delay? Ablating a glutamatergic neuron removes AMPA receptor-mediated input from its synaptic partners but also removes the input mediated by metabotropic glutamate receptors (mGluRs) that regulate phosphoinositide intracellular signaling and maintain robust function of inspiratory burst-generating conductances. Intracellular pharmacology experiments have shown that antagonists of the phosphoinositide signaling system can take 20–40 min to attenuate excitability and burst generation (22, 23). Therefore, the delayed effects of cumulative single-cell laser ablations on cycle period are attributable, at least in part, to the rundown of phosphoinositide signaling after removal of mGluR-mediated drive.

The present results support the hypothesis that laser ablations destroy a critical mass of the preBötC core that precludes rhythm generation. As an additional metric to assess the postlesion state of the CPG, we exploited previous evidence that SP excites NK1R-expressing preBötC neurons to boost respiratory activity (24). Lesioned preBötC-surface slices exhibited irregular SP-evoked rhythms that were unsustainable (Fig. 6 *C* and *D*). We conclude that the cumulative serial ablation leaves the respiratory CPG irreparably damaged.

As a consequence, this study provides a unique measurement that can help quantify network properties of the preBötC: The destruction of 120 ± 45 inspiratory neurons stops the spontaneous respiratory rhythm irreversibly in vitro. An important consideration is that neuroanatomical evidence shows that approximately one-half of the neurons in the preBötC are inhibitory, either glycinergic or GABAergic, and one-half are glutamatergic (13, 25). Glutamatergic transmission is obligatory for rhythmogenesis in vitro (26, 27), whereas inhibitory transmission is not (28, 29). Synaptic inhibition nonetheless regulates the amplitude of XII motor output (10, 11). To focus on the role of glutamatergic neurons, we performed these experiments in the presence of picrotoxin and strychnine. Disinhibition conditions ensured that deleting inhibitory neurons would not affect the XII output. Inspiratory neurons express both excitatory (25, 30–32) and inhibitory (12, 13) transmitters, but it is not possible to differentiate the two phenotypes based on calcium transients in rhythmically active slices. Therefore, approximately one-half of the targets in our experiments are presumably inhibitory and should be discounted from the lesion tally. We conclude that deleting 60 ± 23 glutamatergic neurons (mean ± SD) stopped respiratory rhythmogenesis in vitro.

From the number of inspiratory neurons detected per imaging plane, we may estimate the population of the preBötC core by extrapolating through the volume of the preBötC and correcting for the fraction of cells that are inhibitory. We detected the highest number of inspiratory neurons in the preBötC at −30 μm (13 per side; Table S1). Therefore, we assume that, on average, fewer than 13 neurons were detected at superficial levels because of slicing-related tissue damage, and that fewer than 13 neurons were detected at deeper levels because of limited dye penetration and scattering of laser pulses (33). Even if technical limitations prevented their detection, we assume an average uniform density of 13 inspiratory neurons per 10 μm per side in the preBötC, which occupies 250 μm in the rostrocaudal axis, bilaterally (9, 25, 34). Thus, we calculate 650 inspiratory neurons comprise the preBötC. If one-half are inhibitory (13, 25), then the rhythm-generating glutamatergic core contains 325 interneurons.

These data and calculations imply that destroying 18% (60/325) of the preBötC core, with the 95% confidence intervals of 4% (14/325) to 33% (106/325), stopped the respiratory rhythm. Because bolus injection of SP evoked a transient sequence of XII bursts, connectivity among core neurons must still exist. As a consequence, we conclude that the lesion procedure did not destroy the respiratory rhythm-generating network per se, but destroyed enough of it to preclude sustainable and stable rhythmic function in vitro. It may be possible to restore some functionality to a lesioned preparation by exploiting the remaining unlesioned neurons and their connectivity, but to attempt to do so is beyond the scope of the present study.

Disease Model. Neurodegenerative diseases often present respiratory pathologies ranging from sleep-disordered breathing to respiratory failure (35–38). The loss of brainstem neurons that express neuroanatomical characteristics consistent with the preBötC have been associated with such pathologies (6, 39, 40). We determined that the loss of ≈18% of the preBötC core can stop spontaneous rhythms without completely destroying the underlying network. These results suggest that neurodegenerative disorders may manifest abnormal respiratory behavior and, potentially, respiratory failure, even when relatively small fractions of the respiratory networks that include the preBötC are destroyed during disease progression. The model we present could be used to simulate disease etiology by progressively lesioning a network so that it approaches the tipping point from a nominally functional system to one that can no longer spontaneously function without intervention. The network, thus lesioned in vitro, could be used to develop and evaluate prevention and treatment strategies that bolster respiratory function.

Materials and Methods

The Institutional Animal Care and Use Committee at The College of William and Mary approved these protocols. Neonatal mice aged 0–3 d were anesthetized and dissected in ACSF containing 124 mM NaCl, 3 mM KCl, 1.5 mM $CaCl_2$, 1 mM $MgSO_4$, 25 mM $NaHCO_3$, 0.5 mM NaH_2PO_4, and 30 mM D-glucose, equilibrated with 95% O_2 and 5% CO_2 (vol/vol) at pH = 7.4. Transverse slices (450–500 μm) containing the preBötC were loaded with 36 μM Fluo-8 AM (AAT Bioquest) and perfused with 27 °C ACSF at 4 mL/min. The external K^+ concentration was raised to 9 mM, and inspiratory motor output was recorded from XII nerve roots. Picrotoxin and strychnine (5 μM) were added to the ACSF before the start of the experiments.

Imaging and ablations were performed by using a laser-scanning microscope (Zeiss LSM 510) and a Ti:Sapphire laser (Spectra Physics). Rhythmically active neurons were detected via calcium imaging. Ablations were performed by using the Ti:Sapphire laser to spot-scan cell targets with 800-nm pulses at maximum intensity. We measured XII burst magnitude, cycle period, and CV during pre- and postlesion conditions. We also computed a regularity score (R_n) defined as the quotient of period of the present cycle with respect to the mean cycle period for 10 previous cycles. Each dataset was tested for normality by using a Shapiro–Wilk test. Normally distributed data were compared by using two-tailed paired or unpaired Student's *t* tests, whereas data that did not conform to the normal distribution were compared by using two-tailed nondirectional Mann–Whitney *u* tests. XII burst amplitude (area), cycle period, and CV are reported with SE (mean ± SEM). Discrete cell counts are reported according to the mean and SD (mean ± SD).

Slices were fixed in paraformaldehyde and phosphate buffer after each experiment and then stained with thionin acetate to verify neuroanatomical landmarks.

ACKNOWLEDGMENTS. This work was supported by National Institutes of Health Grant 1 R21 NS070056-01 (to C.A.D.N.).

1. Grillner S (2006) Biological pattern generation: The cellular and computational logic of networks in motion. *Neuron* 52:751–766.
2. Kiehn O (2011) Development and functional organization of spinal locomotor circuits. *Curr Opin Neurobiol* 21:100–109.
3. Feldman JL, Del Negro CA (2006) Looking for inspiration: New perspectives on respiratory rhythm. *Nat Rev Neurosci* 7:232–242.
4. Smith JC, Ellenberger HH, Ballanyi K, Richter DW, Feldman JL (1991) Pre-Bötzinger complex: A brainstem region that may generate respiratory rhythm in mammals. *Science* 254:726–729.
5. Gray PA, Janczewski WA, Mellen N, McCrimmon DR, Feldman JL (2001) Normal breathing requires preBötzinger complex neurokinin-1 receptor-expressing neurons. *Nat Neurosci* 4:927–930.
6. McKay LC, Janczewski WA, Feldman JL (2005) Sleep-disordered breathing after targeted ablation of preBötzinger complex neurons. *Nat Neurosci* 8:1142–1144.
7. Tan W, et al. (2008) Silencing preBötzinger complex somatostatin-expressing neurons induces persistent apnea in awake rat. *Nat Neurosci* 11:538–540.
8. Janczewski WA, Feldman JL (2006) Distinct rhythm generators for inspiration and expiration in the juvenile rat. *J Physiol* 570:407–420.
9. Ruangkittisakul A, Panaitescu B, Ballanyi K (2010) K(+) and Ca(2+) dependence of inspiratory-related rhythm in novel "calibrated" mouse brainstem slices. *Respir Physiol Neurobiol* 175:37–48.
10. Ren J, Greer JJ (2006) Modulation of respiratory rhythmogenesis by chloride-mediated conductances during the perinatal period. *J Neurosci* 26:3721–3730.
11. Ritter B, Zhang W (2000) Early postnatal maturation of GABAA-mediated inhibition in the brainstem respiratory rhythm-generating network of the mouse. *Eur J Neurosci* 12:2975–2984.
12. Kuwana S, et al. (2006) Electrophysiological and morphological characteristics of GABAergic respiratory neurons in the mouse pre-Bötzinger complex. *Eur J Neurosci* 23:667–674.
13. Winter SM, et al. (2009) Glycinergic interneurons are functionally integrated into the inspiratory network of mouse medullary slices. *Pflugers Arch* 458:459–469.
14. Ruangkittisakul A, Okada Y, Oku Y, Koshiya N, Ballanyi K (2009) Fluorescence imaging of active respiratory networks. *Respir Physiol Neurobiol* 168:26–38.
15. Koizumi H, et al. (2008) Functional imaging, spatial reconstruction, and biophysical analysis of a respiratory motor circuit isolated in vitro. *J Neurosci* 28:2353–2365.
16. Barnes BJ, Tuong CM, Mellen NM (2007) Functional imaging reveals respiratory network activity during hypoxic and opioid challenge in the neonate rat tilted sagittal slab preparation. *J Neurophysiol* 97:2283–2292.
17. Smith JC, Greer JJ, Liu GS, Feldman JL (1990) Neural mechanisms generating respiratory pattern in mammalian brain stem-spinal cord in vitro. I. Spatiotemporal patterns of motor and medullary neuron activity. *J Neurophysiol* 64:1149–1169.
18. Ptak K, et al. (2009) Raphé neurons stimulate respiratory circuit activity by multiple mechanisms via endogenously released serotonin and substance P. *J Neurosci* 29: 3720–3737.
19. Liu KS, Fetcho JR (1999) Laser ablations reveal functional relationships of segmental hindbrain neurons in zebrafish. *Neuron* 23:325–335.
20. Bargmann C, Avery L (1995) *Laser Killing of Cells in Caenorhabditis elegans. Caenorhabditis elegans: Modern Biological Analysis of an Organism, Methods in Cell Biology*, eds Epstein H, Shakes D (Elsevier, Amsterdam), Vol 48, pp 225–250.
21. Lechner HA, Lein ES, Callaway EM (2002) A genetic method for selective and quickly reversible silencing of Mammalian neurons. *J Neurosci* 22:5287–5290.
22. Crowder EA, et al. (2007) Phosphatidylinositol 4,5-bisphosphate regulates inspiratory burst activity in the neonatal mouse preBötzinger complex. *J Physiol* 582:1047–1058.
23. Pace RW, Mackay DD, Feldman JL, Del Negro CA (2007) Inspiratory bursts in the preBötzinger complex depend on a calcium-activated non-specific cation current linked to glutamate receptors in neonatal mice. *J Physiol* 582:113–125.
24. Gray PA, Rekling JC, Bocchiaro CM, Feldman JL (1999) Modulation of respiratory frequency by peptidergic input to rhythmogenic neurons in the preBötzinger complex. *Science* 286:1566–1568.
25. Gray PA, et al. (2010) Developmental origin of preBötzinger complex respiratory neurons. *J Neurosci* 30:14883–14895.
26. Wallén-Mackenzie A, et al. (2006) Vesicular glutamate transporter 2 is required for central respiratory rhythm generation but not for locomotor central pattern generation. *J Neurosci* 26:12294–12307.
27. Funk GD, Smith JC, Feldman JL (1993) Generation and transmission of respiratory oscillations in medullary slices: Role of excitatory amino acids. *J Neurophysiol* 70: 1497–1515.
28. Feldman JL, Smith JC (1989) Cellular mechanisms underlying modulation of breathing pattern in mammals. *Ann N Y Acad Sci* 563:114–130.
29. Brockhaus J, Ballanyi K (1998) Synaptic inhibition in the isolated respiratory network of neonatal rats. *Eur J Neurosci* 10:3823–3839.
30. Guyenet PG, Sevigny CP, Weston MC, Stornetta RL (2002) Neurokinin-1 receptor-expressing cells of the ventral respiratory group are functionally heterogeneous and predominantly glutamatergic. *J Neurosci* 22:3806–3816.
31. Stornetta RL, et al. (2003) A group of glutamatergic interneurons expressing high levels of both neurokinin-1 receptors and somatostatin identifies the region of the pre-Bötzinger complex. *J Comp Neurol* 455:499–512.
32. Bouvier J, et al. (2010) Hindbrain interneurons and axon guidance signaling critical for breathing. *Nat Neurosci* 13:1066–1074.
33. Svoboda K, Yasuda R (2006) Principles of two-photon excitation microscopy and its applications to neuroscience. *Neuron* 50:823–839.
34. Ruangkittisakul A, et al. (2006) High sensitivity to neuromodulator-activated signaling pathways at physiological [K+] of confocally imaged respiratory center neurons in on-line-calibrated newborn rat brainstem slices. *J Neurosci* 26:11870–11880.
35. Maria B, et al. (2003) Sleep breathing disorders in patients with idiopathic Parkinson's disease. *Respir Med* 97:1151–1157.
36. Benarroch EE (2007) Brainstem respiratory control: Substrates of respiratory failure of multiple system atrophy. *Mov Disord* 22:155–161.
37. Ferguson KA, Strong MJ, Ahmad D, George CF (1996) Sleep-disordered breathing in amyotrophic lateral sclerosis. *Chest* 110:664–669.
38. Punjabi NM, et al. (2009) Sleep-disordered breathing and mortality: A prospective cohort study. *PLoS Med* 6:e1000132.
39. Benarroch EE (2003) Brainstem in multiple system atrophy: Clinicopathological correlations. *Cell Mol Neurobiol* 23:519–526.
40. Benarroch EE, Schmeichel AM, Low PA, Parisi JE (2003) Depletion of ventromedullary NK-1 receptor-immunoreactive neurons in multiple system atrophy. *Brain* 126: 2183–2190.